Geotextiles and Geomembranes 35 (2012) 25–40

Contents lists available at SciVerse ScienceDirect

Geotextiles and Geomembranes

journal homepage: www.elsevier.com/locate/geotexmem

Predictive modeling on seismic performances of geosynthetic-reinforced soil walls

K.Z.Z. Lee [a,*], N.Y. Chang [b]

[a] Geotechnical Engineering Group, Technical Service Center, U.S. Bureau of Reclamation, Denver Federal Center, Building 67, Denver, CO 80225, USA
[b] Department of Civil Engineering, University of Colorado Denver, 1200 Larimer Street, Room NC3027, Denver, CO 80217, USA

ARTICLE INFO

Article history:
Received 6 January 2012
Received in revised form
29 May 2012
Accepted 21 June 2012
Available online 25 July 2012

Keywords:
Numerical simulation
Prediction
Geosynthetic-reinforced soil
Parametric study
Seismic displacement
Multivariate analysis

ABSTRACT

This paper presents the results of numerical parametric study of free-standing simple geosynthetic-reinforced soil (GRS) walls under real multidirectional ground motion shaking. The predictions were made using a validated finite element computer program. Design parameters, such as (1) wall height, (2) wall batter angle, (3) soil friction angle, (4) reinforcement spacing, and (5) reinforcement stiffness, were evaluated in the study. Prior to the parametric study, the extent of finite element model (FEM) boundary was verified in order to minimize the boundary effect. Results of parametric study were compared against the values determined using the Federal Highway Administration (FHWA) allowable stress design methodology. It was found that the FHWA methodology overestimates the reinforcement tensile load as compared to the FEM results. Multivariate regression equations were developed using FEM results for the various seismic performances based on multiple design parameters that are essential in the design of GRS walls. In particular, the prediction equations for wall facing horizontal displacement, wall crest settlement, and reinforcement tensile load are presented. The prediction equations can provide first-order estimates of the seismic performances of free-standing simple GRS walls.

1. Introduction

The state-of-practice design of geosynthetic-reinforced soil (GRS) wall follows the limit equilibrium design approach (e.g., Elias et al., 2001). In the pseudo-static analysis of GRS walls, only the factors of safety against various modes of failure or collapse of the wall could be estimated, and wall deformation could not be estimated directly from the pseudo-static analysis. This is a common deficiency in all of the limit equilibrium analyses. Indirect methods were developed to estimate the horizontal wall movements (or the time-deformation response of the wall system) to accompany the seismic stability analysis. The widely accepted approach is the Newmark sliding block method (Newmark, 1965). In Newmark's double-integration displacement method applied to retaining wall structure, the total displacement is termed unsymmetrical displacement, since the permanent displacement only accumulates in one direction (outward direction). The calculation of displacement is based on the assumption that the moving mass displaces as a rigid-plastic block with shear resistance mobilized along a potential sliding surface. Permanent displacement of the rigid-plastic block is said to have occurred whenever the forces acting on the soil mass (both static and seismic forces) overcomes the available shear resistance along the potential sliding surface. The permanent displacements are assumed to accumulate each time the ground acceleration exceeds the critical acceleration.

Cai and Bathurst (1996a) had identified three seismic induced sliding mechanisms in a GRS wall, and they are (1) external sliding along the base of the entire wall structure, (2) internal sliding along a reinforcement layer and through the facing column, and (3) block interface shear between facing column units. The displacements are estimated using the conventional sliding block method, and both horizontal acceleration coefficient k_h and vertical coefficient k_v are used to calculate dynamic active forces and are assumed to remain constant through out the entire wall structure. The vertical inertial force is assumed to act upward to produce the most critical factors of safety for the horizontal sliding mechanisms. Another sliding block method proposed by Siddharthan et al. (2004) was based on seismic centrifuge test results of mechanically stabilized earth (MSE) walls, where a rigid-plastic multi-block computational method was developed to predict the permanent displacement of MSE wall subjected to seismic loading. The failure mechanism is comprised of three rigid blocks and possesses a bi-linear failure plane; the top two blocks are rectangular, and the bottom block is triangular.

---

* Corresponding author. Tel.: +1 303 445 3022; fax: +1 303 445 6472.
E-mail address: KLee@usbr.gov (K.Z.Z. Lee).

0266-1144/$ – see front matter Published by Elsevier Ltd.
http://dx.doi.org/10.1016/j.geotexmem.2012.06.005

Ling et al. (1996), on the other hand, suggested the two-part wedge mechanism, which has been used to determine the reinforcement length based on tieback/compound failure or direct sliding failure of a vertical wall. The two-part wedge mechanism was further considered in determining the seismic induced permanent displacement of a reinforced steep slope by Ling et al. (1997) and Leshchinsky (1997). The displacement evaluation procedure is similar to the base sliding approach proposed by Cai and Bathurst (1996a), in which the reinforced soil zone is treated as a rigid-plastic block. The displacement of the rigid-plastic block is induced when the factor of safety against direct sliding is less than unity. Huang et al. (2003) introduced the 'multi-wedge method' (e.g., three-wedge method) to account for the contribution of facing component and the connecting reinforcement force at the facing-backfill interface in evaluating the seismic displacements of GRS walls, where the three-wedge mechanism was considered to be more appropriate for describing the observed failure patterns. The three-wedge method calculates both the horizontal and vertical displacements utilizing the Newmark sliding block theory. Huang et al. (2003) reported that the calculated displacements using the three-wedge method were comparable with the measured values from the Chi-Chi, Taiwan earthquake.

Newmark's double-integration method in finding the seismic induced permanent displacement requires the ground motion time history to be known. In absence of the ground motion time history, several empirical methods have been developed to predict the seismic induced permanent displacement of earth structures (e.g., Whitman and Liao, 1984; Cai and Bathurst, 1996b; Huang and Wu, 2006; Anderson et al., 2008). Newmark's sliding block theory has been used as the basis for developing the empirical methods, where the total permanent displacement determined by Newmark's double-integration method is correlated with input ground motion parameters, such as peak ground acceleration, peak ground velocity, and critical acceleration ratio.

The seismic responses of GRS wall can be examined by means of physical model tests or through a numerical modeling study. It is, however, uneconomical and impractical to examine the seismic responses of GRS wall by conducting a series of full-scale physical tests with different types of soils and reinforcements under various seismic loads. Hence, a more economical and practical approach for examining the seismic responses of GRS wall is to conduct a numerical modeling study, in which the numerical tool would need to be validated from physical model tests under well controlled conditions. A review of numerical simulation on seismic performances of GRS structures is provided in Lee et al. (2010).

This study was performed to examine the seismic performances of free-standing simple GRS walls with uniform reinforcement spacing and constant reinforcement length under real multidirectional seismic shaking through numerical simulation. The validated numerical tool with proven predictive capability was used to perform a parametric study, where design parameters, such as wall height, wall batter angle, soil friction angle, reinforcement spacing, and reinforcement stiffness, were evaluated. The results of the numerical parametric study were compared with values determined from the Federal Highway Administration (FHWA) allowable stress design methodology (Elias et al., 2001), and discrepancies between the two were identified. The results of the numerical parametric study provided the data needed to develop seismic performance prediction equations. Prediction equations for wall facing horizontal displacement, wall crest settlement, and reinforcement tensile load were developed based on multivariate regression analysis. The prediction equations can provide first-order estimates of the seismic performances in the preliminary analysis of free-standing simple GRS walls.

2. Numerical modeling

The general purpose nonlinear finite element computer program LS-DYNA (Hallquist, 1998) was selected for the numerical analysis. LS-DYNA can be used to analyze large deformation and dynamic response of solids and structures. The program utilizes explicit central difference method to integrate the equations of motion in time. The available elements include 4-node tetrahedron and 8-node solid elements, 2-node beam elements, 3- and 4-node shell elements, 8-node thick shell elements, and rigid bodies. LS-DYNA includes many built-in material models to simulate a wide range of material behaviors including elasticity, plasticity, composites, thermal effects and rate dependence. Also included in LS-DYNA is the contact interface capability. The contact-impact algorithm can solve contact problems, such as frictional sliding with closure and separation, single surface contact, arbitrary mechanical interactions between independent bodies, and in draw beads in metal stamping applications.

In essence, validation of a computer program requires the comparison between the calculated results and the measured data from a physical model test. The shaking table tests performed by Ling et al. (2005a) were selected as the validation experiments, since they were full-scale models and that detail descriptions of backfill, reinforcement, and interface properties were provided. Materials considered in the validation assessment include concrete facing block, expanded polystyrene (EPS) board, geogrid reinforcement, and backfill. Concrete facing blocks and EPS boards were simulated as linear elastic materials. EPS boards were placed in the front end and at the back end of the full-scale shaking table models as dampers. The density ρ of EPS board of 15 kg/m^3 was based on ASTM C578 Type I material. The maximum shear modulus of EPS is approximately 2.76 MPa. With an assumed Poisson's ratio ν of 0.4, the Young's modulus E of EPS was calculated to be 7.72 MPa. The facing block was assigned with typical concrete elastic properties ($E = 2320$ kg/m^3, $E = 25$ GPa, $\nu = 0.15$). Geogrid reinforcement and soil are simulated by the plastic-kinematic model and the geologic cap model, respectively; descriptions of these models are presented in the material characterization sections below.

The LS-DYNA validation assessment and quality of simulation have been reported in Lee et al. (2010). As an example, Fig. 1 shows the comparison of the calculated and measured displacement time histories for one of the test walls. Through the validation assessment, it was found that strong inference or high confidence is anticipated for the closely matched responses, such as horizontal wall displacement and lateral earth pressure utilizing the calibrated model. Variability within the measured data is thought to have contributed to some of the comparison discrepancies. With the computer program validated, prediction can thus be made with strong inference. The relationship between validation and prediction pertaining to geotechnical problems has been discussed in Lee et al. (2011). Note that the prediction could not indicate the accuracy of a complex system that has not been validated; rather the accuracy could only be inferred based on the previous quantitative comparison.

2.1. Input ground motions

A total of 20 earthquake records were selected for the parametric study. The earthquake records were obtained from the Pacific Earthquake Engineering Research Center (PEER) Strong Motion Database (http://peer.berkeley.edu/smcat/). The earthquake records for the parametric study were selected primarily based on the peak horizontal acceleration (PHA) as it is the primary design parameter in the seismic design of GRS walls. The PHA's of the selected records range from 0.114 g to 0.990 g.

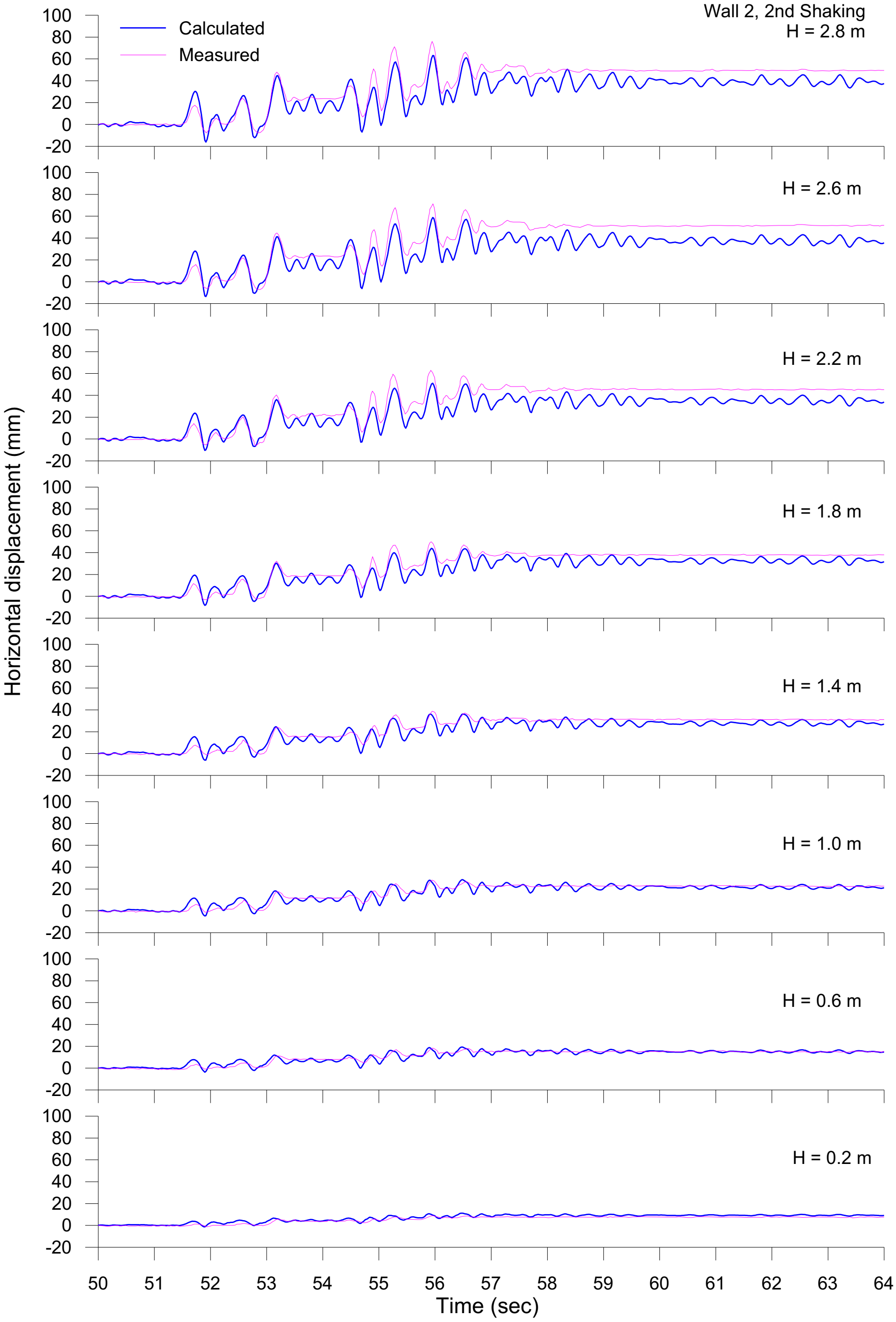

Fig. 1. Comparison of wall face displacement time histories in validation assessment.

The 20 selected records are all free-field motions with the instrumentation located at the ground surface. The geotechnical subsurface characteristics for the 20 records ranged from shallow to deep soil profiles. The ground motion parameters (including duration, peak acceleration, peak velocity, and peak displacement) of the selected earthquake records are summarized in Table 1. Also included in Table 1 are the fault type and the moment magnitude M_W of each earthquake record. The selected records were baseline corrected using the computer program BAP (Converse and Brady, 1992) to eliminate possible drifts. The peak values presented in Table 1 are based on the baseline corrected records. Note that deconvolution of the records from the ground surface to the base of numerical model in the parametric study was not performed, since the depth to the base of the model is considered shallow (i.e., less than 7 m).

Variation of peak vertical acceleration (PVA) with PHA for the 20 records is shown in Fig. 2. As illustrated by Fig. 2, most of the records are bounded between the 1V:1H and 1/3V:1H slopes. Three of the records have PVA higher than PHA. The fault type associated with each record is also indicated in Fig. 2. The three records having higher PVA than PHA are associated with reverse fault.

2.2. Soil characterization

Granular soils were considered in the parametric study. The friction angle ϕ' is of significant importance in describing the

Table 1
Ground motion parameters of the 20 earthquake records.

No.	Earthquake	PEER record		Date	Duration (s)	Peak acc.		Peak velocity		Peak disp.		Fault type	M_w
		ID	File			Hor. (g)	Vert. (g)	Hor. (cm/s)	Vert. (cm/s)	Hor. (cm)	Vert. (cm)		
1	Duzce, Turkey	P1557	1062-N	1999/11/12	30.02	0.114	0.093	11.08	7.66	9.28	8.04	Strike-Slip	7.1
2	Oroville	P0115	D-EBH000	1975/08/08	13.65	0.168	0.073	3.07	1.67	0.17	0.06	Normal	4.7
3	Kobe, Japan	P1054	SHI090	1995/01/16	35.03	0.212	0.059	27.90	6.40	7.71	2.57	Strike-Slip	6.9
4	Coyote Lake	P0149	G03140	1979/08/06	26.815	0.229	0.160	28.75	5.18	4.86	1.26	Strike-Slip	5.7
5	Kobe, Japan	P1054	SHI000	1995/01/16	35.03	0.243	0.059	37.76	6.40	8.86	2.57	Strike-Slip	6.9
6	Coalinga	P0346	H-Z14000	1983/05/02	40.02	0.282	0.097	40.85	11.38	8.10	4.11	Reverse	6.4
7	Northridge	P0887	ARL090	1994/01/17	40.04	0.344	0.552	40.44	17.73	15.06	8.54	Reverse	6.7
8	Loma Prieta	P0736	G03090	1989/10/18	30.01	0.367	0.338	45.00	15.02	20.26	9.03	Reverse-Oblique	6.9
9	Loma Prieta	P0745	CLS090	1989/10/18	30.01	0.479	0.455	45.11	17.65	11.26	7.12	Reverse-Oblique	6.9
10	Northridge	P0883	ORR360	1994/01/17	40.04	0.514	0.217	52.04	12.29	15.52	5.22	Reverse	6.7
11	Cape Mendocino	P0810	RIO360	1992/04/25	36.04	0.549	0.195	41.90	10.54	19.74	7.04	Reverse	7.1
12	Northridge	P0883	ORR090	1994/01/17	40.04	0.568	0.217	51.82	12.29	8.86	5.22	Reverse	6.7
13	Loma Prieta	P0745	CLS000	1989/10/18	30.01	0.644	0.455	55.29	17.65	10.62	7.12	Reverse-Oblique	6.9
14	Kobe, Japan	P1056	TAZ000	1995/01/16	38.02	0.694	0.433	67.80	34.76	30.91	11.92	Strike-Slip	6.9
15	Chi-Chi, Taiwan	P1461	TCU095-N	1999/09/20	60.015	0.712	0.255	49.39	22.02	26.95	19.20	Reverse-Oblique	7.6
16	Northridge	P1020	SPV270	1994/01/17	24.44	0.753	0.467	84.47	33.02	18.70	9.74	Reverse	6.7
17	Northridge	P1005	RRS228	1994/01/17	14.96	0.838	0.852	166.02	50.63	28.07	11.96	Reverse	6.7
18	Northridge	P1023	SCS142	1994/01/17	40.01	0.897	0.586	102.20	34.59	45.12	25.67	Reverse	6.7
19	Chi-Chi, Taiwan	P1532	WNT-E	1999/09/20	50.015	0.958	0.311	68.60	34.16	32.08	16.70	Reverse-Oblique	7.6
20	Northridge	P0935	TAR360	1994/01/17	40.04	0.990	1.048	77.17	73.46	30.21	21.66	Reverse	6.7

behavior of granular material, thus it was used as the primary parameter for developing other physical properties. The three selected values of ϕ' are 32°, 36°, and 40°. The physical properties of the granular material were developed using ϕ' based on various references (Peck et al., 1974; Kulhawy and Mayne, 1990; NAVFAC, 1986a,b) and are summarized in Table 2. The relative density D_r could be expressed in terms of percent or relative compaction (RC) according to the relation suggested by Lee and Singh (1971) as: $RC = 80 + 0.2 \times D_r$, where D_r is expressed in percentage. Values of RC for the three soils are included in Table 2. Note that even though the $\phi' = 32°$ soil has a RC of 89%, this study does not suggest soil compaction be done at RC of 89%, where the norm of practice is a RC of 95%. Values of RC in Table 2 merely reflect the probable range of values based on published relationships.

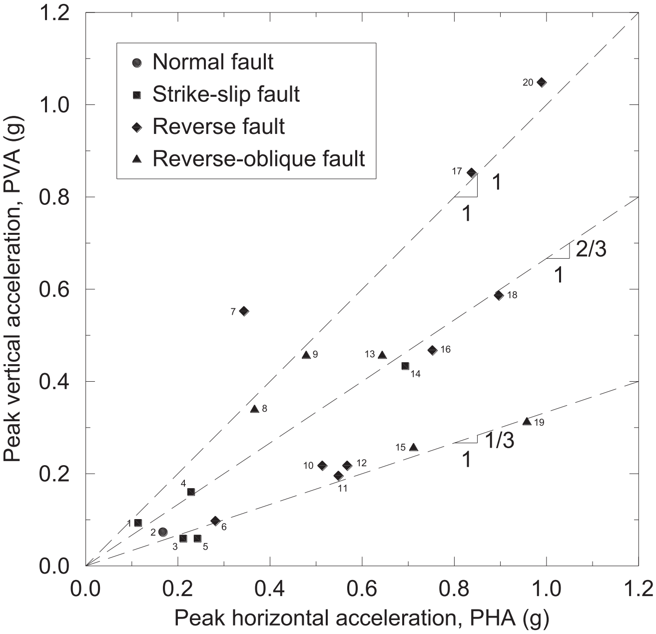

Fig. 2. Variation of peak vertical acceleration with peak horizontal acceleration for the 20 selected earthquake records.

2.2.1. Cap model strength parameters in parametric study

The soil was represented by the geologic cap model. The cap model is situated in the $\sqrt{J_2}$:I_1 stress space, where I_1 is the first invariant of the stress tenor and J_2 is the second invariant of the deviatoric stress tensor (see Fig. 3). Cap model is comprised of a fixed yield surface f_1 and a yield cap f_2. The fixed yield surface f_1 is considered as the failure surface, where region above the failure surface is not permissible. The expression for f_1, originally adopted by DiMaggio and Sandler (1971) and later modified by Sture et al. (1979), is given as:

$$f_1 = \sqrt{J_2} + \gamma e^{-\beta I_1} - \theta I_1 - \alpha = 0 \tag{1}$$

where α, β, γ, and θ are the material parameters. The yield cap f_2 is a moving yield surface. The moving yield cap follows the shape of an ellipse and is represented by:

$$f_2 = R^2 J_2 + (I_1 - C)^2 = R^2 b^2 \tag{2}$$

where R is termed the shape factor and is the ratio of the major axis to minor axis of the ellipse, and $Rb = (X - C)$. X is the value of I_1 at the intersection of the yield cap and the I_1-axis, C is the value of I_1 at the center of the ellipse, and b is the value of $\sqrt{J_2}$ when $I_1 = C$. X is a hardening parameter that controls the change in size of the moving yield surface and the magnitude of the plastic deformation, and X depends on the plastic volumetric strain ε_v^p through:

$$X = -\frac{1}{D}\ln\left(1 - \frac{\varepsilon_v^p}{W}\right) + X_o \tag{3}$$

where D, W, and X_o are the material parameters. Note that W characterizes the ultimate plastic volumetric strain, D denotes the total volumetric plastic strain rate, and X_o determines the initiation of volumetric plastic deformation under hydrostatic loading conditions

Table 2
Physical properties of soils used in parametric study.

ϕ' (°)	N (blows/0.3 m)	D_r (%)	γ_d (kN/m^3)	USCS	w (%)	γ_m (kN/m^3)	ρ (kg/m^3)	RC (%)
32	16	44	16.2	SP	16.5	18.9	1926.6	89
36	30	65	18.5	SW	12.5	20.8	2120.3	93
40	45	80	20.9	GP	12.5	23.5	2395.5	96

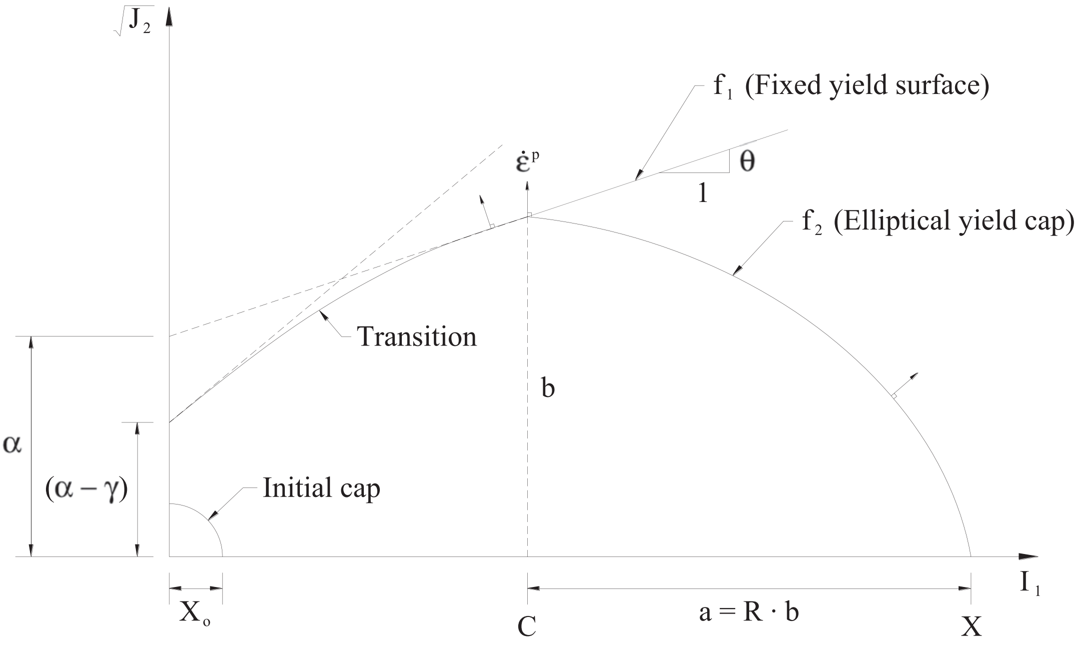

Fig. 3. Schematic of geologic cap model.

(Zaman et al., 1982). X_0 can also be thought as the preconsolidation hydrostatic pressure. The stress state inside the yield surfaces is considered to exhibit elastic behavior. The descriptions of cap model along with other geologic constitutive models under general loading conditions were summarized by Ko and Sture (1981).

Two strength parameters required by the geologic cap model are α and θ, which govern the location of the fixed yield surface f_1. Adopting the Drucker–Prager failure criterion and matching the compressive meridian of the Mohr–Coulomb criterion, the strength parameters α and θ can be related to c' and ϕ' through:

$$\alpha = \frac{6c' \cos\phi'}{\sqrt{3}(3 - \sin\phi')} \tag{4}$$

$$\theta = \frac{2\sin\phi'}{\sqrt{3}(3 - \sin\phi')} \tag{5}$$

A minimal value of c' equal to 5 $\mathrm{kN/m^2}$ was assumed for all three soils in the parametric study. The small value of c' was added to provide numerical stability during finite element calculations. Cap model failure envelope exponential coefficient γ and exponent β were further assumed to be zero so that f_1 takes the same form as the Drucker–Prager failure criterion. The cap model strength parameters for the three soils are summarized in Table 3.

2.2.2. *Cap model hardening parameters in parametric study*

Determination of cap model hardening parameters required by Eq. (3) followed the procedure provided previously by Lee et al. (2010). The hardening parameters were developed based on the assumed relative densities D_r of the three soils. The cap model hardening parameters for the three soils are summarized in Table 3. The parameters needed to determine mean stress dependent variables such as K_t, G, and D for the three soils are summarized in Table 4. Variations of mean stress dependent variables K_t, G, and D with depth for the three soils are shown in Fig. 4. As indicated in Fig. 4, nonlinear response is observed with increasing depth for the mean stress dependent variables. Variation of R with mean stress is provided in Lee et al. (2010).

The stress–strain curves were generated from numerical triaxial test utilizing a single element model under axisymmetric loading condition. The single element model was first subjected to hydrostatic compression pressure σ_3 (or mean stress p) and subsequently subjected to the application of deviatoric stress $\Delta\sigma$. The loading condition was consistent with the consolidated-drained conventional triaxial compression test. Fig. 5 shows the stress–strain curves of the three soils at the same confining pressure of 70 kPa. Stiffer stress–strain response is observed for the soil with $\phi' = 40°$, and during shearing, the $\phi' = 40°$ soil also contracts less in volumetric strain than the $\phi' = 32°$ soil. The pattern is consistent with realistic soil behavior with the notion that stiffer response is associated with the higher strength soil.

2.3. *Geosynthetic reinforcement characterization*

Three geogrid reinforcements were devised for the parametric study. The tensile load–strain responses of the three geogrids were estimated based on results of various geogrid tensile load tests as shown in Fig. 6, and the three geogrids were termed accordingly based on their stiffness characteristics. The high strength geogrid exhibits the near upper-bound tensile load–strain response, whereas the low strength geogrid reflects closely the lower-bound tensile load–strain response. The medium strength geogrid is

Table 3
Cap model parameters for the three soils of parametric study.

Parameter	$\phi' = 32°$	$\phi' = 36°$	$\phi' = 40°$
Bulk modulus, K_t (MPa) (see Fig. 4)	Vary with p	Vary with p	Vary with p
Shear modulus, G (MPa) (see Fig. 4)	Vary with p	Vary with p	Vary with p
Failure envelope parameter, α (kPa)	5.9	5.8	5.6
Failure envelope linear coefficient, θ	0.2477	0.2814	0.3149
Failure envelope exponential coef., γ	0	0	0
Failure envelope exponent, β $(\mathrm{kPa})^{-1}$	0	0	0
Shape factor, R (see Lee et al., 2010)	Vary with p	Vary with p	Vary with p
Hardening law exponent, D (see Fig. 4)	Vary with p	Vary with p	Vary with p
Hardening law coefficient, W	0.0401	0.0277	0.0189
Hardening law exponent, X_o (kPa)	0	0	0

Table 4
Parameters for finding mean stress dependent variables K_t, G, and D for the three soils of parametric study.

Parameter	$\phi' = 32°$	$\phi' = 36°$	$\phi' = 40°$
Relative density, D_r (%)	44	65	80
Initial tangent bulk modulus, K_i (kPa)	6089	8982	11,049
Asymptotic total volumetric strain, $(\varepsilon_v)_{asy}$	0.0445	0.0307	0.0209
Ultimate total volumetric strain, $(\varepsilon_v)_{ult}$	0.0423	0.0292	0.0199
Ultimate tangent bulk modulus, $(K_t)_{ult}$ (MPa)	2436	3593	4419
Ultimate elastic volumetric strain, $(\varepsilon_v^e)_{ult}$	0.0021	0.0015	0.001
Ultimate plastic volumetric strain, $(\varepsilon_v^p)_{ult} = W$	0.0401	0.0277	0.0189

viewed as having the average load–strain response. The three geogrids were assumed to have a constant thickness of 1.5 mm. The geogrids were simulated by the plastic-kinematic model, which describes a bilinear stress–strain response. Description of the bilinear stress–strain model was provided in Lee et al. (2010). The slope of tensile load–strain curve is the product of modulus (e.g., Young's modulus E or tangent modulus E_t) and thickness of the geogrid. The tensile load is expressed in units of force per unit width of the reinforcement. Inversely, modulus was calculated by dividing the slope of the tensile load–strain curve by the geogrid thickness. Similarly, the yield stress σ_y for the bilinear model was found by dividing the yield tensile load by the thickness of geogrid. The model parameters for the three geogrids are summarized in Table 5. It should be noted that no failure criterion is implemented in the plastic-kinematic model, thus a geogrid rupture failure cannot occur. Reinforcement tensile load at 5% strain ($T_{5\%}$) was selected to represent the stiffness characteristic, since $T_{5\%}$ is readily available from product specifications (e.g., IFAI, 2011). Values of $T_{5\%}$ for the three geogrids adopted in the study are included in Fig. 6.

2.4. Development of model dimensions

Free-standing simple GRS wall was considered in the parametric study. The models in the parametric study were developed based on dimensions defined in Fig. 7. The length of the retained earth behind the reinforced soil mass was extended beyond the theoretical static passive slip plane. Similarly, the length of the foundation soil in front of the wall was also extended beyond the static passive slip plane emanating from the lower left boundary of the model. The extent of the boundaries alongside the model was adopted in order to minimize interference between the model boundary and the potential formation of slip surfaces. For comparison, the extents of numerical models from other research studies are summarized in Table 6.

The depth of the foundation soil was selected to be 0.75 of the wall height as it is the minimum boring depth required for a subsurface investigation (Arman et al., 1997). It was further assumed that competent bedrock underlies the foundation soil. This minimal foundation soil depth conforms to the assumption that the wall is situated in a competent site, where problematic foundation soils that might lose their strengths when subjected to seismic loads do not exist (e.g., liquefiable soils). The groundwater table was assumed to be below the bottom of the foundation soil, and the deep groundwater table does not affect the seismic performance of the wall. In the parametric study, granular soil was assumed as the backfill for the reinforced soil mass. In addition, it was assumed that on-site material was used to construct the wall; hence all soils including the reinforced soil, retained earth, and the foundation soil would exhibit similar behavior. Only one soil type was specified in each numerical wall model.

The effect of lateral extent of the vertical side boundaries on the seismic response of GRS wall was evaluated. The evaluation was conducted on a 6 m high, 10° wall facing batter, 0.4 m reinforcement spacing, and $\phi' = 36°$ wall. The depth of foundation soil was kept constant at 0.75 of the wall height, while the extent of the vertical side boundaries was changed to 0.5 and 1.5 times of the proposed extent. The three models were subjected to the same Northridge earthquake shaking (i.e., No. 12, P0883, ORR090) with peak horizontal and vertical accelerations of 0.568 g and 0.217 g, respectively. The calculated maximum horizontal displacement

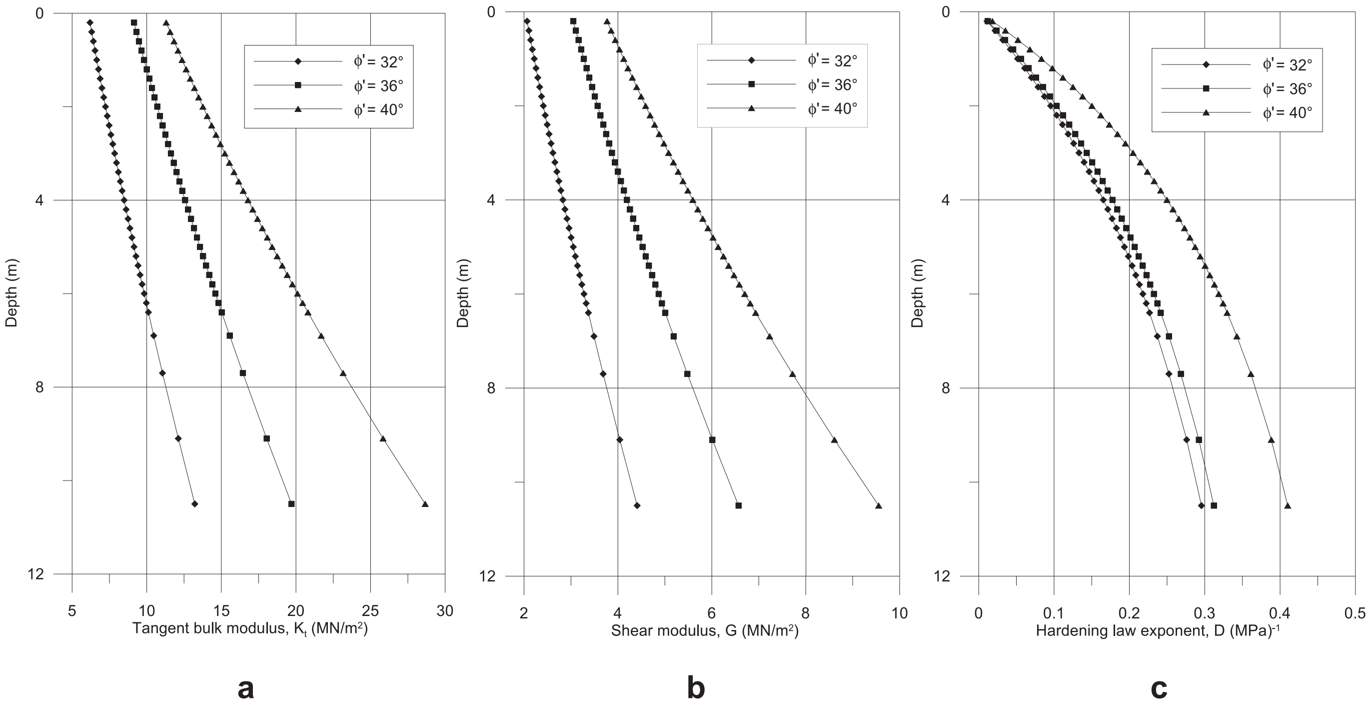

Fig. 4. Variation of (a) tangent bulk modulus K_t, (b) shear modulus G with depth, (c) hardening law exponent D with depth.

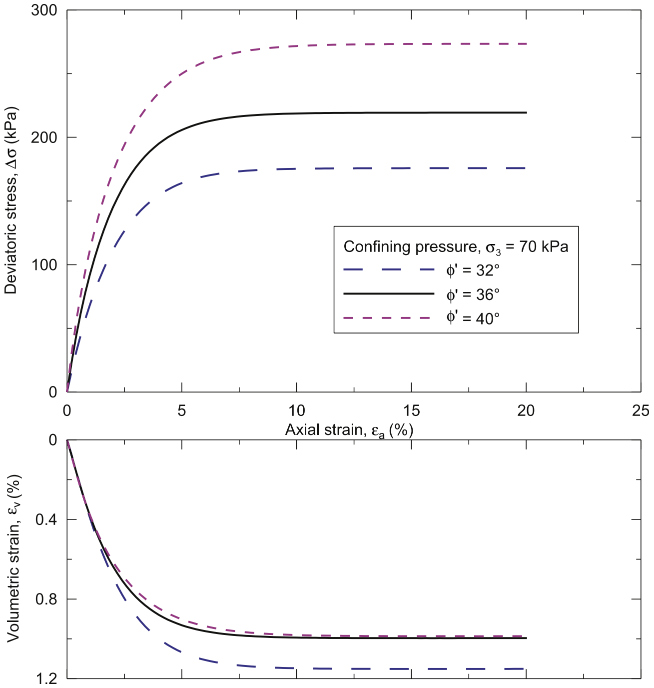

Fig. 5. Triaxial compression stress–strain curves of three granular soils at confining pressure of 70 kPa.

Table 5
Plastic–kinematic model parameters for geogrid reinforcements.

Parameter	High stiffness	Medium stiffness	Low stiffness
Density, ρ (kg/m^3)	1030	1030	1030
Young's modulus, E (MPa)	1155.6	533.3	160
Poisson's ratio, ν	0.3	0.3	0.3
Yield stress, σ_y (MPa)	34.7	21.3	8
Tangent modulus, E_t (MPa)	656.4	266.7	35.6

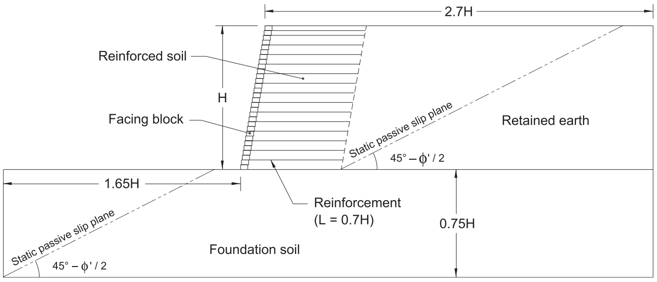

Fig. 7. Numerical model dimensions adopted in the parametric study.

profiles are presented in Fig. 8. As indicated in the figure, the model with 0.5 times the proposed extent experienced the least amount of horizontal displacement, and the models of the proposed extent and 1.5 times the proposed extent experienced larger horizontal displacements. However, the variation in horizontal displacement is minimal between the proposed extent and that of the 1.5 times the proposed extent. The results indicated that the interference of vertical side boundaries to the response of the model diminishes with the distance beyond the proposed extent of the vertical side boundaries. The proposed boundary extent was thus considered adequate and was adopted in the parametric study.

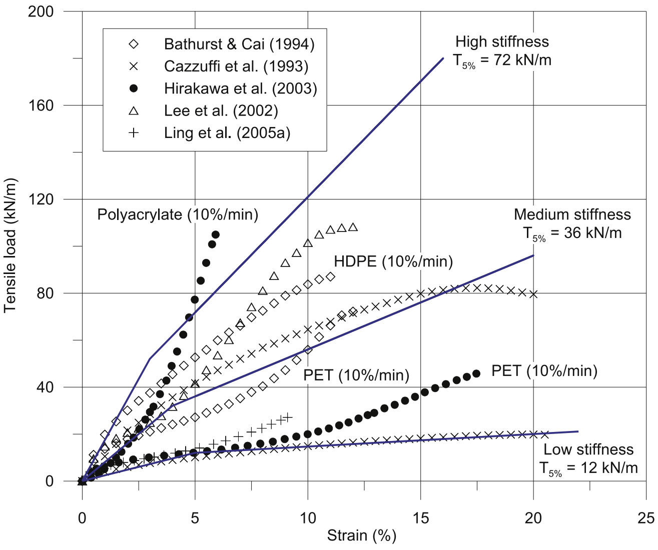

Fig. 6. Comparison of tensile load test results between idealized geogrids and typical geogrids Bathurst and Cai, 1994; Cazzuffi et al., 1993; Hirakawa et al., 2003; Lee et al., 2002..

3. Parametric study program

The purposes of the parametric study were to examine the parameters that could affect the seismic responses of GRS walls and to determine the extent of influence a particular parameter might have on the seismic responses. The parameters considered include (1) wall height H, (2) wall batter angle ω, (3) soil friction angle ϕ', (4) reinforcement spacing S_v, and (5) reinforcement stiffness $T_{5\%}$. These parameters are basic features and components in the construction of a GRS wall, which are also considered as the primary parameters in the design of such wall system. The parametric study program is shown schematically in Fig. 9. A total of 11 models were developed for the parametric study.

For each of the parameters examined, the baseline case was encompassed by a lower value and a higher value. The selected parameter values are typical of free-standing GRS wall having simple wall geometry. Generic facing block dimension was used, where the width and the height of block were conveniently assumed to be 0.3 m and 0.2 m, respectively. For all 11 models, a uniform reinforcement length of 0.7 times the wall height was specified as the ratio of 0.7 is recommended in the FHWA design guidelines. Although the ratio of 0.7 may not yield the most cost

Table 6
Summary of numerical model boundary extents from wall facing adopted by various researchers (H = wall height).

Reference	Numerical model boundary extent from wall facing		
	Front of wall	Back of wall	Foundation depth
Bathurst and Hatami (1998)	0.375H	6.667H	0.167H
Hatami and Bathurst (2000)	0.272H	6H	0.111H
Ling et al. (2005b)	1.667H	3.38H	0.5H
Liu et al. (2011)	1.875H	3.125H	0.625H
Rowe and Ho (1998)	–	2.5H	–
Rowe and Skinner (2001)	1.263H	1.863H	1.263H
This study	1.65H	2.7H	0.75H

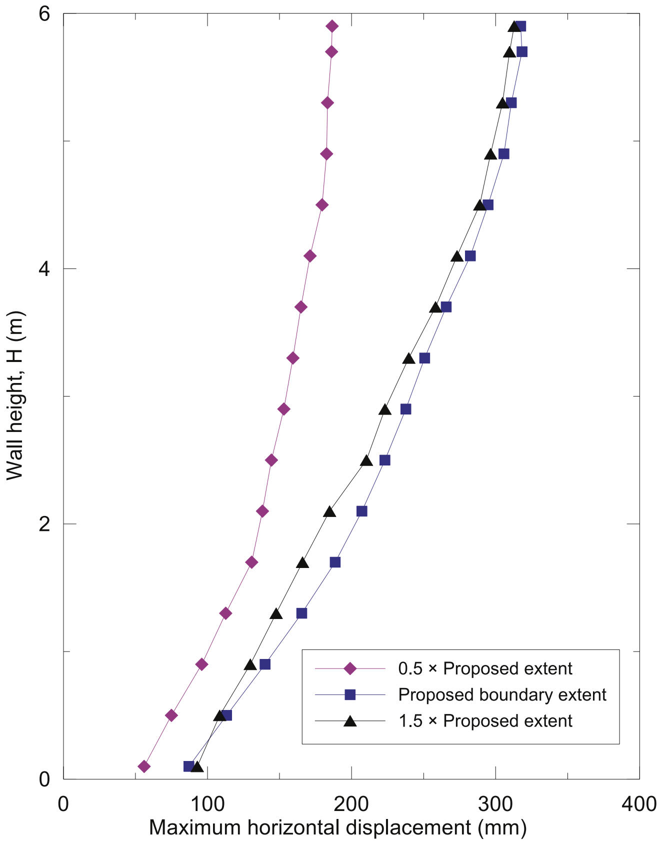

Fig. 8. Effect of lateral boundary extent on wall displacement.

effective wall system, it is anticipated that a significant reduction of the ratio could possibly result in wall instability and lead to adverse performances.

The modeling procedure for the parametric study is identical to the procedure described previously in Lee et al. (2010). Same as the validation process, the parametric numerical models were analyzed under plane strain condition. Two types of elements were used to discretize the numerical models. The facing blocks, reinforced soil, retained earth, and foundation soil were discretized with 8-node constant stress solid elements. The geogrid reinforcements were discretized with 4-node Belytschko–Tsay shell elements, and one integration point was assigned in the shell element that allows no bending resistance. The numerical model can be thought of as an extremely large scale shaking table test. Similar to a shaking table test, buffer material that has the same material properties of EPS was placed in the front and at the back of the model. The EPS material was also modeled with the solid elements.

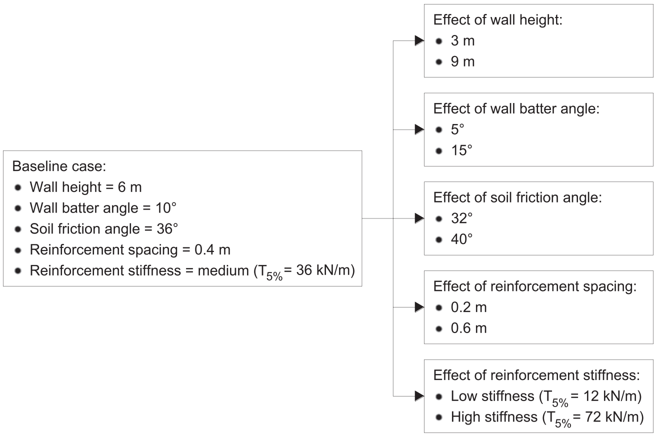

Fig. 9. Parametric study program.

Table 7
Summary of coefficient of friction for contact interfaces.

Contact	$\phi' = 32°$	$\phi' = 36°$	$\phi' = 40°$
Concrete–soil	0.42	0.48	0.56
Concrete–concrete	0.5	0.5	0.5
Geogrid–concrete	0.5	0.5	0.5
Geogrid–soil	0.42	0.48	0.56
EPS–soil	0.42	0.48	0.56

In the numerical model, gravity was simulated as a body load and was applied at the onset of the analysis (i.e., gravity turn-on method). The body load takes the form of a step function and was maintained at the constant gravitation acceleration throughout the duration of seismic loading. Note that a quiet period of 12 s was sustained after the application of gravity load before the beginning of seismic loading in order to damp the model and to reach quasi-static condition. The seismic loading was simulated by prescribing the horizontal and vertical acceleration time histories to the vertical side boundary nodes and nodes at the base of the model. Another quiet period of 12 s was added at the end of seismic loading to again bring the model to a stable condition.

Contact interfaces were specified between two distinct parts within the model. By including the thickness of geogrid reinforcement in the model, element incompatibility occurs in the backfill at the end of geogrid layer. The “tied-surface-to-surface” contacts were used to tie the incompatible backfill elements. The contact interface is defined by the coefficient of friction μ, and μ for contacts with soil was estimated using $\mu = 2/3 \cdot \tan\phi'$. Values of μ adopted in the parametric study are summarized in Table 7. Note that as a dry stack modular block wall, no mechanical connections were used to connect the facing block and the reinforcement; connection was based solely on the interface frictional resistance.

As an example, the model geometry and the locations where performances were recorded for the baseline model are shown in Fig. 10a, and the corresponding finite element mesh is shown in Fig. 10b. Note that embedment depth at the toe of the wall was not considered. The minimum wall embedment depth of 0.5 m is suggested in the FHWA design methodology. Stability of the wall model is expected to increase if the embedment depth is incorporated in the model. The results without considering the embedment depth would thus be more conservative.

4. Results of parametric study

Results of parametric study were analyzed through statistical means to determine relationships between the seismic performances of free-standing simple GRS walls and the various design parameters. Multivariate linear regression analysis was performed to determine prediction equations of seismic performances. The regression analysis utilized the curve-fitting technique, where the best-fit prediction equations were developed using the least squares method based on the available finite element model (FEM) data. The least squares solution requires that the sum of squared deviations of the predicted values from the actual observed values is at a minimum. In this study, the seven design parameters, including (1) the peak horizontal acceleration PHA, (2) peak vertical acceleration PVA, (3) wall height H, (4) wall batter angle ω, (5) effective soil friction angle ϕ', (6) reinforcement spacing S_v, and (7)

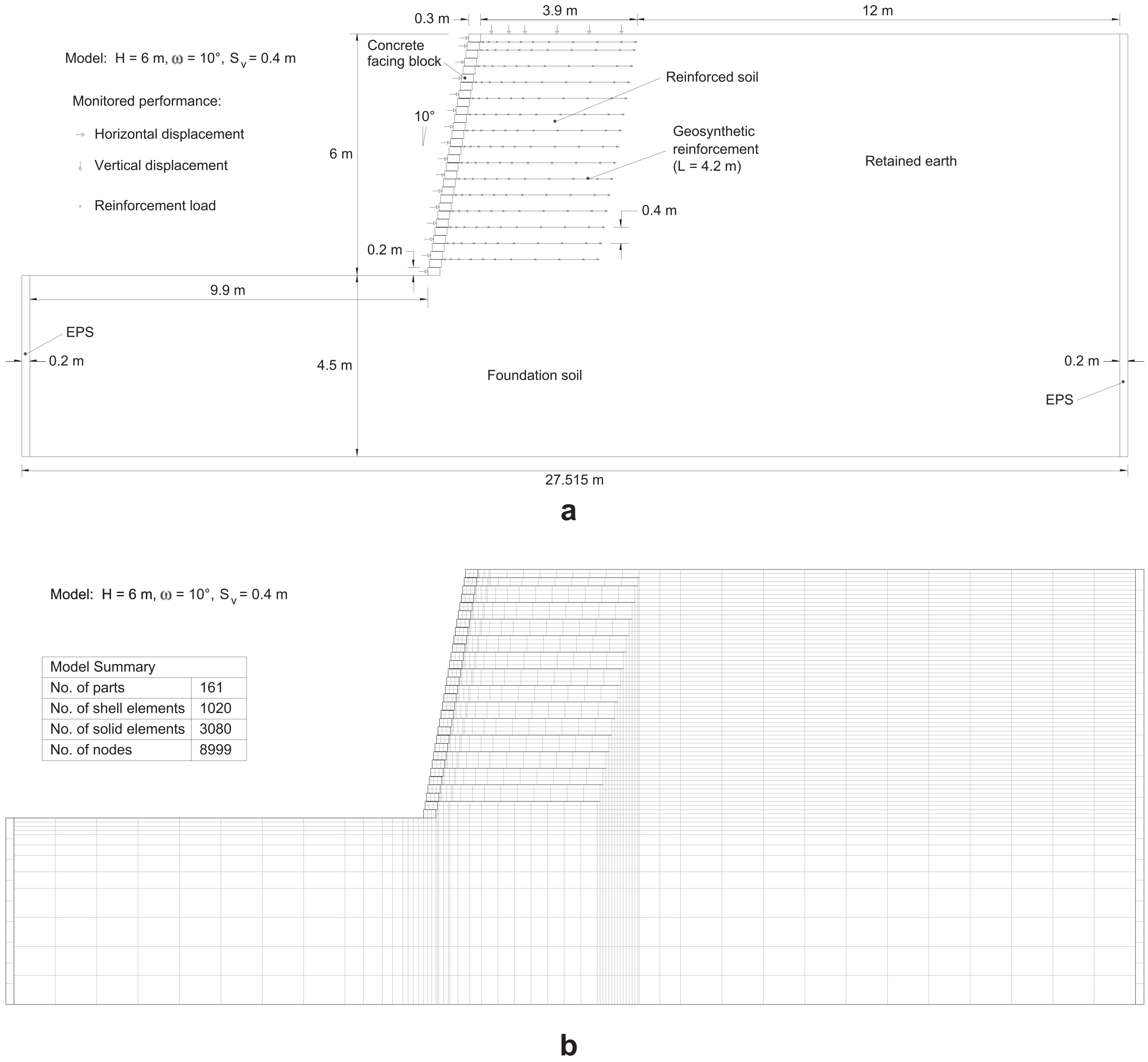

Fig. 10. Configuration of the 6 m wall with (a) dimensions and materials and (b) finite element mesh of model.

reinforcement stiffness $T_{5\%}$, are considered as the independent variables (or predictor variables). The dependent variables are the FEM calculated seismic performances, such as (1) the maximum horizontal displacement $\varDelta_h$, (2) maximum crest settlement $\varDelta_v$, and (3) maximum reinforcement tensile load T_{total}.

The results indicated that all seismic performances show nonlinear relationship with design parameter PHA. The nonlinear response is expected given nonlinear material behavior, contact interface interaction, and complex loading pattern simulated in the numerical model. The observed nonlinear response can readily be described by the exponential function. As such, it is then appropriate to take the natural logarithm of the seismic performances to be the values of dependent variables in the multivariate linear regression analysis. The multivariate linear regression equation with transformed dependent variable is defined as:

$$\ln(Y) = b_0 + b_1X_1 + b_2X_2 + b_3X_3 + b_4X_4 + b_5X_5 + b_6X_6 + b_7X_7 \tag{6}$$

where Y = dependent variable, $\ln(Y)$ = transformed dependent variable, $X_1, X_2, \ldots, X_7$ = independent variables, b_0 = constant, and $b_1, b_2, \ldots, b_7$ = regression coefficients. Eq. (6) can be expressed in terms of design parameters as:

$$\ln(Y) = b_0 + b_1\mathrm{PHA} + b_2\mathrm{PVA} + b_3H + b_4\omega + b_5\phi' + b_6S_v + b_7T_{5\%} \tag{7}$$

The prediction equation, which is an exponential function, is found by taking the inverse of the natural logarithmic function of Eq. (7) as:

$$Y = \exp\left(b_0 + b_1\mathrm{PHA} + b_2\mathrm{PVA} + b_3H + b_4\omega + b_5\phi' + b_6S_v + b_7T_{5\%}\right) \tag{8}$$

The exponent of the prediction equation consists of a linear combination of the independent variables with coefficients resulted from the regression analysis. The results of regression analysis, including R^2 value, for predicting seismic performances of GRS walls are summarized in Table 8. The units of predictors PHA, PVA, H, ω, ϕ', S_v, and $T_{5\%}$ are g (gravitational acceleration), g, meter,

Table 8
Summary of constant and regression coefficients from the multiple regression analysis [$Y = \exp\,(b_0 + b_1\mathrm{PHA} + b_2\mathrm{PVA} + b_3H + b_4\omega + b_5\,\phi' + b_6S_v + b_7T_{5\%})$].

Response Y	Constant b_0	Regression coefficients							R^2
		b_1	b_2	b_3	b_4	b_5	b_6	b_7	
Δ_h (mm)	2.900	4.578	0.330	0.251	−0.0192	−0.0434	0.0553	−0.00239	0.710
Δ_v (mm)	1.397	3.056	0.380	0.272	−0.0222	−0.0246	0.6102	−0.00909	0.727
T_{total} (kN/m)	0.748	1.158	0.437	0.185	−0.0109	−0.0209	1.194	0.0153	0.854

degree, degree, meter, and kN/m, respectively. Units of seismic performances Δ_h, Δ_v, and T_{total} are millimeter, millimeter, and kN/m, respectively.

The prediction equations established using the exponential function do not pass through the origin, since a zero intercept violates the exponential function. Use of the exponential function inevitably introduces finite amount of response at very low values of PHA. However, the exponential correlations were considered representative of the FEM results within the range of conditions evaluated in the parametric study.

4.1. *Effects of wall height*

Three wall heights of 3 m, 6 m, and 9 m were evaluated in the parametric study. The seismic responses of maximum horizontal displacement and maximum reinforcement tensile load for the three wall heights are compared in Figs. 11 and 12, respectively. As indicated by these figures, it is apparent that all seismic responses increase in magnitude with increasing wall height in both the FEM results and the FHWA analysis values. Note that the regression curves presented in the comparisons were calculated with PVA assumed to be to 1/3 of PHA in order to show the trends of the prediction equations.

As indicated by the regression curves in Figs. 11 and 12, the rates of increasing responses for the 9 m wall are higher than those of the 3 m wall. This suggests that tall walls are more susceptible to higher PHA than the short walls. The horizontal displacement contours at the end of the analysis for the 9 m wall subjected to the most severe seismic loading out of the 20 earthquake records (i.e., No. 20, P0935, TAR360) is presented in Fig. 13. Top portion of the wall experienced greater horizontal displacement than the bottom portion of the wall. In addition, the reinforced soil mass as a whole translated in the horizontal direction and tended to separate from the retained earth. Toppling of top wall facing blocks was imminent for the 9 m wall at the end of earthquake shaking with a PHA of 0.990 g. The 9 m wall would have failed in toppling of facing blocks if the reinforcements were absent. Note that failure wedges can be seen in the displacement contours of Fig. 13, and the pattern is consistent with the two-part wedge failure observed in the physical model test (e.g., Koseki et al., 2006; Matsuo et al., 1998).

Due to the assumption in finding the maximum horizontal acceleration coefficient A_m [$A_m = (1.45 - A)A$; A = peak acceleration coefficient ≤ 0.29], the FHWA analysis values reach maximum at PHA = 0.725 g and decrease thereafter resulting in concave downward curves. The reinforcement tensile loads calculated by FEM were lower than the FHWA analysis values for PHA up to approximately 0.7 g (see Fig. 12); note that the FHWA analysis values greater than the limitation of 0.29 g are depicted by dashed lines. In other words, FHWA methodology provides a conservative estimate for the reinforcement tensile load. Similar findings have been reported by Allen et al. (2003) and Bathurst et al. (2005) in field case histories, where static reinforcement tensile loads estimated based on measured strains were lower than the FHWA analysis values. FEM results presented in this study could serve as the lower-bound values for design considerations.

4.2. *Effects of wall batter angle*

Three wall batter angles of 5°, 10°, and 15° were evaluated in the parametric study. The seismic responses of maximum horizontal displacement for the three wall batter angles are compared in Fig. 14. As indicated by the results, all the responses increase in magnitude with decreasing wall batter angle in both the FEM results and the FHWA analysis values. The results imply that GRS wall tends to be less stable with decreasing wall batter angle (e.g., near vertical wall facing).

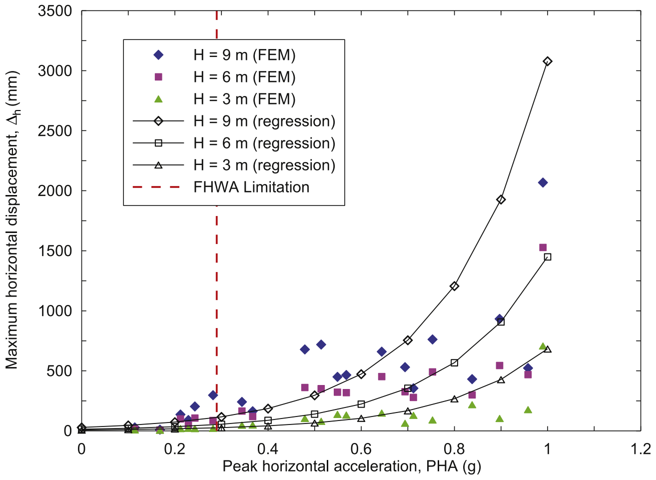

Fig. 11. Effect of wall height on maximum horizontal displacement.

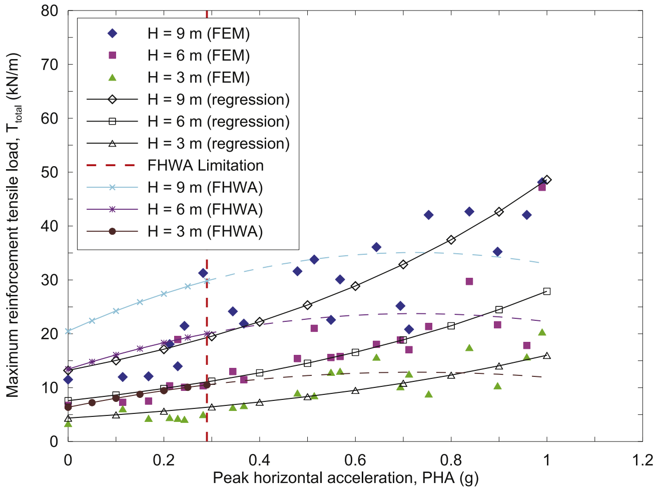

Fig. 12. Effect of wall height on maximum reinforcement tensile load.

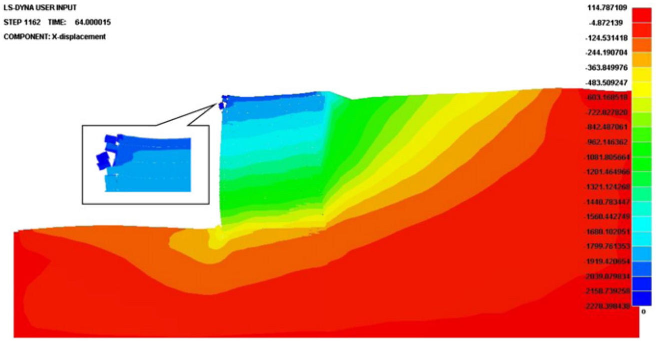

Fig. 13. Contours of horizontal displacement at end of analysis with Northridge Earthquake (No. 20, P0935, TAR360) of model: $H = 9$ m, $S_v = 0.4$ m, $\omega = 10°$, $\phi' = 36°$, $T_{5\%} = 36$ kN/m.

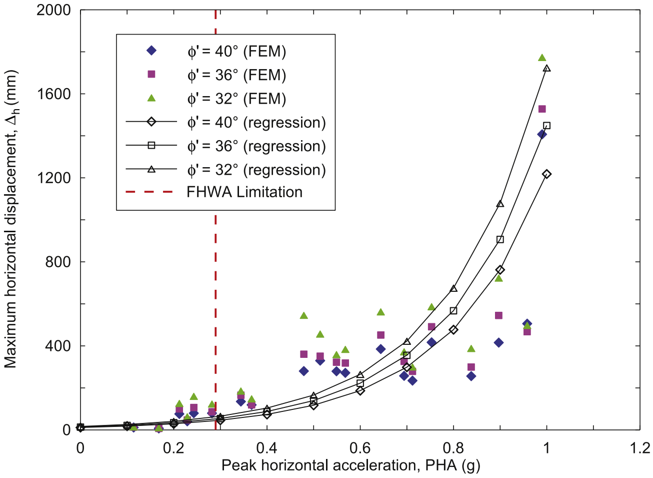

Fig. 15. Effect of soil friction angle on maximum horizontal displacement.

4.3. *Effects of soil friction angle*

Three soil friction angles of 32°, 36°, and 40° were evaluated in the parametric study. The seismic responses of maximum horizontal displacement for the three soil friction angles are compared in Fig. 15. The results indicate that the magnitudes of seismic responses increase with decreasing friction angle as the stiffness of the soil is directly proportional to friction angle (see Fig. 5 for soil behavior). The calculated displacements and settlements are in agreement with the notion that a GRS wall built using higher friction angle backfill would be more stable than that of a lower friction angle backfill. Note also that the maximum reinforcement tensile loads calculated by FEM follow the trend where the tensile load increases with decreasing friction angle, which is in agreement that reinforcement tensile loads are expected to be higher for the case with a lower friction angle backfill.

4.4. *Effects of reinforcement spacing*

Three reinforcement vertical spacings of 0.2 m, 0.4 m, and 0.6 m were evaluated in the parametric study. The seismic responses of maximum crest settlement and maximum reinforcement tensile load for the three reinforcement spacings are compared in Figs. 16 and 17, respectively. The FEM results indicate that uniform reinforcement spacing with value between 0.2 m and 0.6 m enables a coherent composite to be created, and that the maximum horizontal displacement is not significantly affected by the reinforcement spacing. It should be noted that small reinforcement spacing, however, has added benefits to the wall system, such as better quality control of backfill compaction (i.e., due to smaller lift thickness) and more tolerable against potential creep of geosynthetics.

Based on the FEM results, effect of spacing is more pronounced in wall crest settlement and reinforcement tensile load than the horizontal displacement. Magnitudes of wall crest settlement and reinforcement tensile load are proportional to the reinforcement spacing. Small reinforcement spacing of 0.2 m is an effective method in reducing crest settlement and reinforcement tensile load. The reinforcement tensile loads calculated by FEM are lower than the FHWA analysis values for spacings of 0.4 m and 0.6 m; FEM results are higher than the FHWA values for spacing of 0.2 m for PHA greater than approximately 0.5 g (see Fig. 17).

4.5. *Effects of reinforcement stiffness*

Three geogrids with tensile loads at 5% axial strain of 12 kN/m, 36 kN/m, and 72 kN/m were evaluated in the parametric study. The three tensile loads at 5% strain reflect the stiffnesses of the reinforcement (see Fig. 6 for reinforcement behavior), where reinforcements with $T_{5\%}$ of 12 kN/m, 36 kN/m, and 72 kN/m are

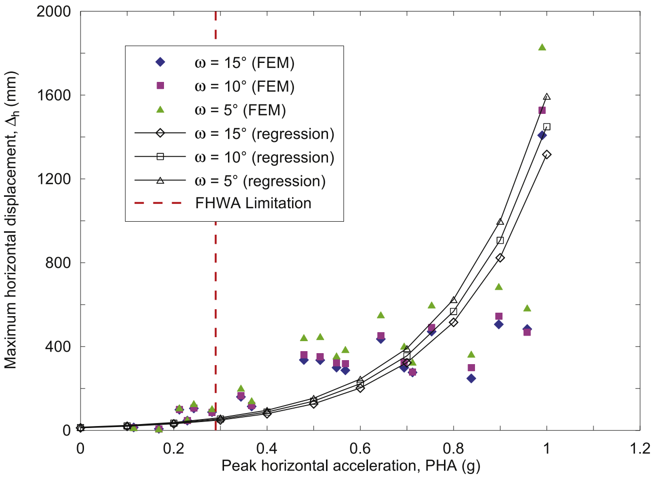

Fig. 14. Effect of wall batter angle on maximum horizontal displacement.

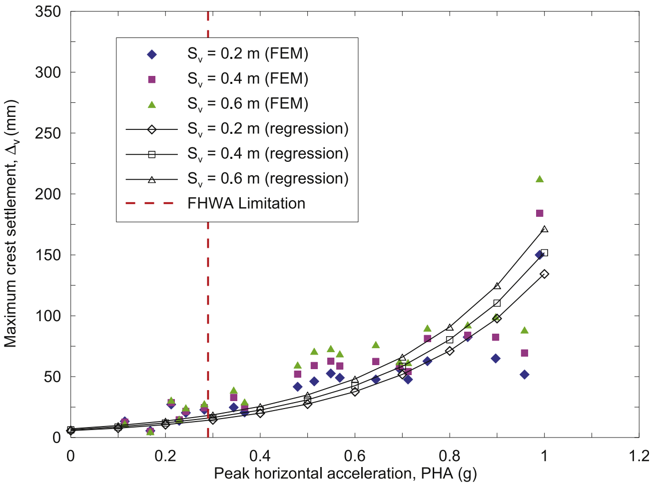

Fig. 16. Effect of reinforcement spacing on maximum crest settlement.

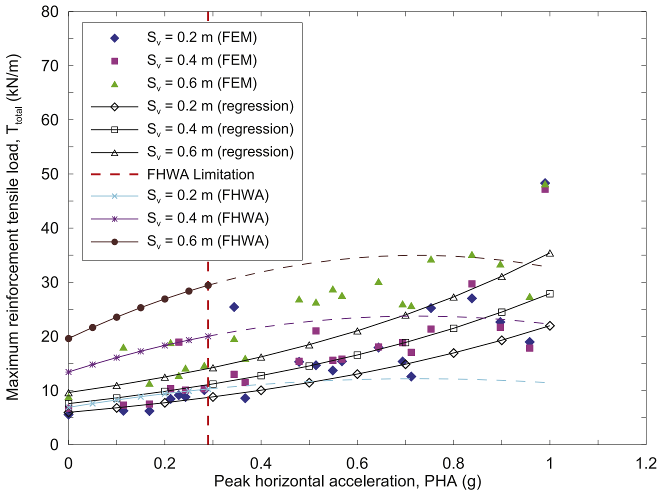

Fig. 17. Effect of reinforcement spacing on maximum reinforcement tensile load.

considered as having low, medium, and high stiffnesses, respectively. The seismic responses of maximum reinforcement tensile load for the three reinforcement stiffnesses are compared in Fig. 18.

Reinforcement stiffness is not addressed by the FHWA methodology as it is not considered in the limit equilibrium analysis. The effect of reinforcement stiffness can only be assessed using finite element analysis or other numerical methods. As indicated by the FEM results, the magnitudes of horizontal displacement and crest settlement increase with decreasing reinforcement stiffness, and the reverse is true for the maximum reinforcement tensile load. Horizontal facing displacement and crest settlement can be controlled effectively by utilizing high stiffness reinforcement. The high stiffness reinforcement, nonetheless, would experience higher reinforcement tensile load than the low stiffness reinforcements when experiencing similar displacement.

The maximum reinforcement tensile loads from the low and medium stiffness reinforcements calculated by FEM are lower than those from the FHWA methodology. However, the maximum reinforcement tensile load with high reinforcement stiffness surpasses the FHWA analysis value at PHA greater than about 0.4 g, which makes the FHWA methodology less conservative for PHA greater than 0.4 g if high stiffness reinforcements were utilized (see Fig. 18).

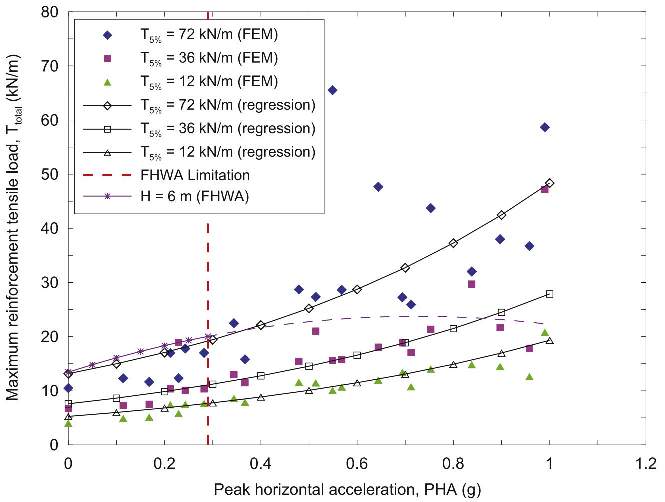

Fig. 18. Effect of reinforcement stiffness on maximum reinforcement tensile load.

4.6. Distribution of reinforcement tensile load

Reinforcement tensile load is needed in the evaluation of GRS wall internal stability. In the parametric study, the maximum reinforcement tensile loads calculated by FEM are in general lower than the FHWA analysis values. This section presents the distribution of tensile load within the reinforced soil mass. In the FHWA methodology, a linear slip surface based on Coulomb's active failure wedge is assumed to pass through the reinforced soil mass. FHWA methodology further assumes that the slip surface coincide with the line of maximum reinforcement tensile load. The anticipated tension distribution along a reinforcement layer takes the shape of a bell curve with the maximum value anchored at the intersection of slip surface and the reinforcement layer; tensile load decreases at increasing distance away from the intersection. The tensile load contours from the load distribution assumed by FHWA methodology will result in a "ridge" within the reinforced soil mass that slopes downward toward top of the wall along the slip surface.

The baseline model analyzed using the Northridge earthquake record (No. 12, P0883, ORR090) with PHA of 0.568 g was processed to generate reinforcement tensile load distribution plots. The effect of seismic shaking is illustrated in the maximum tension lines and the contours plots shown in Fig. 19. Under static condition, the tensile load is concentrated near the wall facing for the top 3/4 of the reinforcements, and the maximum tension line bulges into the reinforced soil mass for the bottom 1/4 of the reinforcements (see Fig. 19a); top reinforcements experienced near zero tension toward the back of the wall (see Fig. 19b). Under seismic condition, all reinforcements experienced higher tensile load than the static condition. The pattern of tension distribution is similar to the static condition, where tensile load is concentrated near the wall facing for the top 3/4 of the reinforcements. However, the maximum tension line for the bottom 1/4 of the reinforcements shifted further inward the reinforced soil mass as compared to the static condition (see Fig. 19a). High reinforcement tensile loads in the bottom 1/4 of the reinforcement indicate that the reinforcements restrain the backfill from lateral translation; stated differently, the reinforcements prevent the backfill from kicking outward. Also, an increase in tensile load in the top reinforcements toward the back of the wall was observed between the static and seismic cases indicating that these reinforcements contribute to the seismic stability of the wall even though the reinforcements have near zero tension under static condition (see Fig. 19c).

Both the maximum tension line and the contours of tensile load are different between the FHWA methodology and those calculated by FEM. A distinct linear maximum tension line is not substantiated by the FEM results. In addition, the tensile load contours based on FEM results are very different and are more complex than the simple "ridge" suggested by the FHWA methodology. If one were to apply the "ridge" analogy to the FEM results, there could be multiple slip surfaces within the reinforced soil mass.

4.7. Design considerations

The prediction equations provided herein (see Table 8) are considered as alternatives to the FHWA methodology for assessing seismic performances of free-standing simple GRS walls. The prediction equations are applicable for conditions similar to those considered in the parametric study and when PHA is greater than the limit of 0.29 g set forth by the FHWA methodology. The earthquake induced maximum horizontal displacement Δ_h and the maximum crest settlement Δ_v are most likely to take place near the top of the wall and close to the wall facing, respectively. The maximum reinforcement tensile load T_{total} is associated with the lower most layer and is located near the mid-length behind the wall facing.

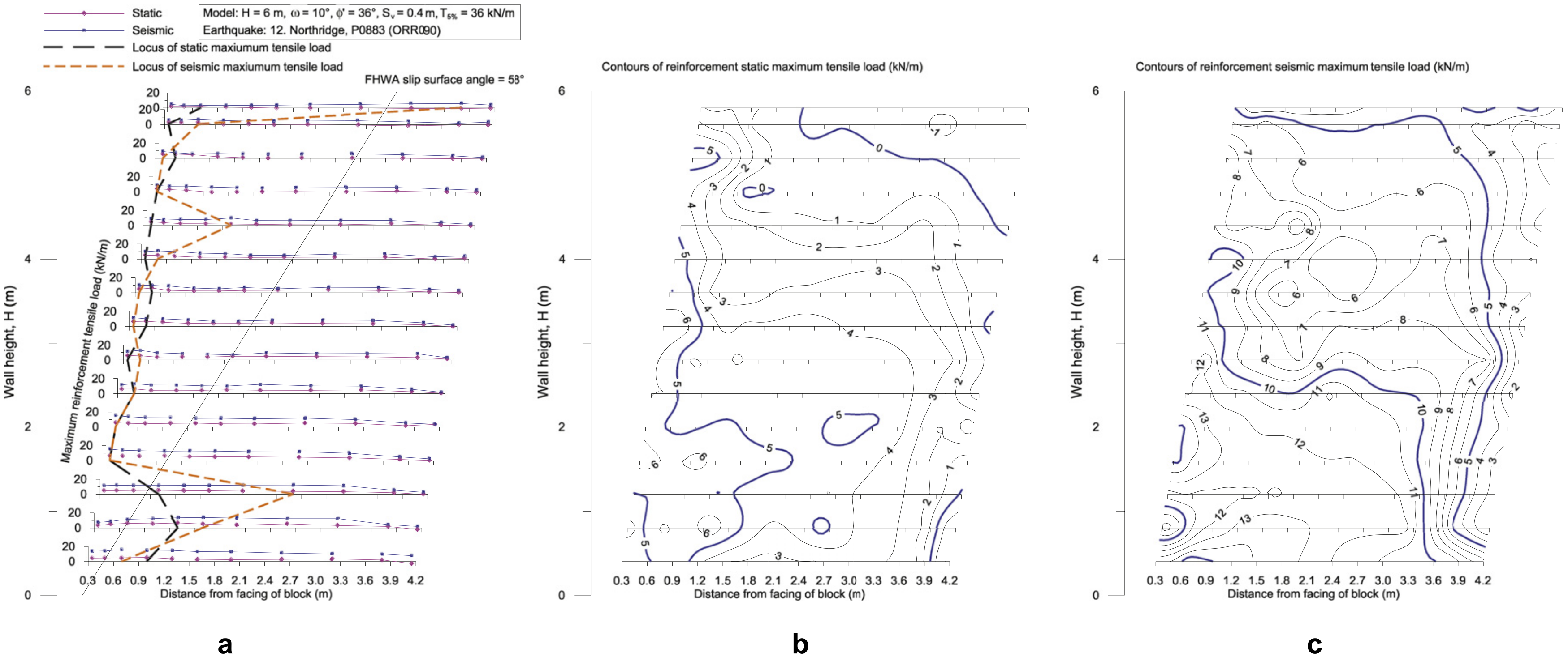

Fig. 19. Distribution of FEM reinforcement tensile load: (a) along individual layer, (b) contours of static tensile load, and (c) contours of seismic tensile load.

Table 9
Change in seismic response of GRS wall due to increase in design parameter.

Design parameter	Seismic response		
	Δ_h	Δ_v	T_{total}
↑ H	↑ (1)	↑ (1)	↑ (1)
↑ ω	↓ (3)	↓ (4)	↓ (5)
↑ ϕ'	↓ (2)	↓ (5)	↓ (4)
↑ S_v	↑ (6)	↑ (3)	↑ (3)
↑ $T_{5\%}$	↓ (4)	↓ (2)	↑ (2)
↑ PVA	↑ (5)	↑ (6)	↑ (6)

Using the prediction equations, seismic performances can be computed rapidly for evaluation in both the ultimate limit state design and the serviceability limit state design. For the serviceability limit states design, deformation tolerance expressed in terms of horizontal displacement-to-wall height ratio (or verticality) from the various guidelines were summarized by Bathurst et al. (2010) and Huang et al. (2009). A value of 5% has been suggested by Koseki et al. (1998) and Huang et al. (2009) as the limiting verticality. The limiting facing displacement could also be governed by the required clearance to the adjacent structures found at the project site. With the prediction equations, it is possible to correlate maximum reinforcement tensile load with the maximum horizontal displacement. A designer could use the prediction equations to estimate the maximum reinforcement tensile load within the GRS wall when the required horizontal displacement or limiting verticality is given from the project site.

5. Conclusions

Seismic performances of free-standing simple GRS walls were evaluated using a validated FEM computer program. A parametric study program was performed to assess the effectiveness of different design parameters (viz., PHA, PVA, H, ω, ϕ', S_v, and $T_{5\%}$). Seismic performances evaluated include wall facing maximum horizontal displacement, maximum wall crest settlement, and maximum reinforcement tensile load. Each case in the parametric study was subjected to 20 free-field earthquake records with PHA ranging from 0.114 g to 0.990 g and PVA ranging from 0.093 g to 1.048 g. Results of parametric study were then compared against the corresponding values determined using the FHWA design methodology.

Multivariate regression analysis was performed using the results of the FEM parametric study to determine prediction equations of the seismic performances based on the design parameters. The prediction equations are applicable to conditions similar to those considered in the parametric study and can provide the first-order estimates of the seismic performances given the various design parameters. In addition, the prediction equations allow seismic performances to be estimated for PHA beyond the limitation of FHWA methodology (i.e., 0.29 g). In applying the prediction equations and when PVA is not available, one could assume PVA to be equal to $1/3 \cdot$PHA to $2/3 \cdot$PHA in order to capture the effects of realistic seismic loading.

The relationships between increases in the design parameters and the resulting seismic responses of GRS walls are summarized in Table 9. In Table 9, an upward pointing arrow (↑) indicates increase in value, and a downward pointing arrow (↓) indicates decrease in value. Also included in Table 9 is the order of significance (or extent of influence) of the design parameter to the individual seismic response ranging from 1 to 6. A number 1 in parenthesis indicates the most significant design parameter that could affect the seismic response, whereas a number 6 in parenthesis indicates the design parameter of least significance. Note that PHA is not included in Table 9 as it is the primary design parameter, and the wall responses are always proportional to PHA. Table 9 could assist a designer for selecting appropriate design parameters based on project's need.

The findings and conclusions drawn from this study include:

1. Failure of GRS walls due to toppling of top facing blocks is more likely than other failure modes. Seismic stability of GRS walls can be improved by joining the top two or three courses of facing block with grout or using other mechanical stabilization mechanism.
2. In the numerical models, failure wedges were noted in the horizontal displacement contours in the retained earth behind the reinforced soil mass, and the pattern is consistent with the two-part wedge failure observed in the physical model tests.
3. GRS walls are less stable at a small batter angle (e.g., near vertical wall).
4. Wall crest settlement and reinforcement tensile load are positively related to the reinforcement spacing. Small reinforcement spacing of 0.2 m is an effective method in reducing crest settlement and reinforcement tensile load.
5. An increase in tensile load in the top reinforcements toward the back of the wall was observed between the static and seismic conditions indicating that these reinforcements contribute to the seismic stability of the wall.
6. Although reinforcement maximum tension line under static condition is not exactly identical to the maximum tension line under seismic condition, both are close to the wall facing. The maximum tension line, in general, is located close to the facing blocks for the top 3/4 of the reinforcements. The maximum tension line shifts toward the mid-length of the reinforcement for the bottom 1/4 of the reinforcements, which results in a high reinforcement tensile load mound at the toe of the wall.
7. The reinforcement tensile loads calculated by FEM are, in general, lower than the FHWA analysis values. The reinforcement stiffness was incorporated in the prediction equation for estimating maximum reinforcement tensile, which is not considered in the FHWA design methodology.
8. The linear slip surface that passes through the reinforced soil mass assumed by the FHWA methodology could not be substantiated with the FEM results. The assumption that the maximum tension line coincides with the linear slip surface is also not supported by the FEM results. In other words, a distinct linear slip surface could not be identified from the FEM results. As suggested by the FEM results, multiple slip surfaces may exist within the reinforced soil mass.
9. In light of maximum tension line being close to the wall facing, connection strength is the prevalent failure mode in the internal stability evaluation.

Acknowledgements

This academic research work was performed during the first writer's Student Career Experience Program (SCEP) with the U.S. Bureau of Reclamation. The career opportunity is gratefully acknowledged. The writers also wish to thank the anonymous reviewers for their critical comments and suggestions.

Nomenclature

A	peak horizontal acceleration coefficient
A_m	design acceleration coefficient
b	minor axis radius of moving yield cap (kN/m^2)
b_0	regression constant
$b_1 \ldots b_7$	regression coefficients

C	cap center stress along I_1 axis (kN/m^2)
c'	drained cohesion (kN/m^2)
D	hardening law exponent (m^2/MN)
D_r	relative density
E	Young's modulus (MN/m^2)
E_t	tangent modulus (MN/m^2)
f_1	fixed yield surface or failure envelope
f_2	elliptical yield cap
G	shear modulus (MN/m^2)
H	wall height (m)
I_1	first invariant of stress tensor (kN/m^2)
J_2	second invariant of deviatoric stress tensor ([kN/m^2]^2)
K_i	initial bulk modulus (MN/m^2)
K_t	tangent bulk modulus (MN/m^2)
$(K_t)_{ult}$	ultimate tangent bulk modulus (MN/m^2)
k_h	horizontal acceleration coefficient; same as A
k_v	vertical acceleration coefficient
L	reinforcement length (m)
M_w	moment magnitude
N	standard penetration number (blows/0.3 m)
PHA	peak horizontal acceleration (gravitational acceleration g)
PVA	peak vertical acceleration (gravitational acceleration g)
p	mean stress (kN/m^2); same as σ_3
R	shape factor or cap axis ratio
RC	relative compaction (%)
S_v	reinforcement vertical spacing (m)
T_{total}	maximum reinforcement tensile load (kN/m)
$T_{5\%}$	reinforcement tensile load at 5% strain (kN/m)
w	moisture content
W	hardening law coefficient
X	cap tip (vertex) stress along I_1 axis (kN/m^2)
X_o	preconsolidation hydrostatic pressure (kN/m^2)
$X_1 \ldots X_7$	independent (or predictor) variable
Y	dependent variable
α	failure envelope parameter (kN/m^2)
β	failure envelope exponent (m^2/kN)
Δ_h	maximum wall facing horizontal displacement (mm)
Δ_v	maximum wall crest settlement (mm)
$\Delta\sigma$	deviatoric stress (kN/m^2)
γ	failure envelope exponential coefficient (kN/m^2)
γ_d	dry unit weight of soil (kN/m^3)
γ_m	moist unit weight of soil (kN/m^3)
ε_a	axial strain
ε_v	total volumetric strain
ε_v^p	plastic volumetric strain
$(\varepsilon_v)_{asy}$	asymptotic total volumetric strain
$(\varepsilon_v)_{ult}$	ultimate total volumetric strain
$(\varepsilon_v^e)_{ult}$	ultimate elastic volumetric strain
$(\varepsilon_v^p)_{ult}$	ultimate plastic volumetric strain; same as W
θ	failure envelope linear coefficient
μ	coefficient of friction
ν	Poisson's ratio
ρ	mass density (kg/m^3)
ϕ'	drained soil friction angle (degree)
σ_3	confining stress (kN/m^2); same as p
σ_y	yield stress (MN/m^2)
ω	wall batter angle (degree)

Abbreviation

EPS	expanded polystyrene
FEM	finite element model
FHWA	Federal Highway Administration
GRS	geosynthetic-reinforced soil
MSE	mechanically stabilized earth
PEER	Pacific Earthquake Engineering Research
USCS	Unified Soil Classification System

References

Allen, T.M., Bathurst, R.J., Holtz, R.D., Walters, D., Lee, W.F., 2003. A new working stress method for prediction of reinforcement loads in geosynthetic walls. Canadian Geotechnical Journal 40 (5), 976–994.

Anderson, D.G., Martin, G.R., Lam, I., Wang, J.N., 2008. Seismic Analysis and Design of Retaining Walls, Buried Structures, Slopes, and Embankments. National Cooperative Highway Research Program, NCHRP Report 611. Transportation Research Board, Washington, D.C., 137 pp.

Arman, A., Samtani, N., Castelli, R., Munfakh, G., 1997. Geotechnical and Foundation Engineering Module 1 – Subsurface Investigations. FHWA-HI-97-021. National Highway Institute, Federal Highway Administration, Washington, D.C., 305 pp.

Bathurst, R.J., Cai, Z., 1994. In-isolation cyclic load-extension behavior of two geogrids. Geosynthetics International 1 (1), 1–19.

Bathurst, R.J., Hatami, K., 1998. Seismic response analysis of a geosynthetic-reinforced soil retaining wall. Geosynthetics International 5 (1–2), 127–166.

Bathurst, R.J., Allen, T.M., Walters, D.L., 2005. Reinforcement loads in geosynthetic walls and the case for a new working stress design method. Geotextiles and Geomembranes 23 (4), 287–322.

Bathurst, R.J., Miyata, Y., Allen, T.M., 2010. Facing displacements in geosynthetic reinforced soil walls. Earth Retention Conference 3. In: Finno, R.J., Hashash, Y.M.A., Arduino, P. (Eds.), ASCE Geotechnical Special Publication No. 208, Proceedings of the 2010 Earth Retention Conference, Bellevue, Washington, August 2010, pp. 442–459.

Cai, Z., Bathurst, R.J., 1996a. Seismic-induced permanent displacement of geosynthetic-reinforced segmental retaining walls. Canadian Geotechnical Journal 33 (6), 937–955.

Cai, Z., Bathurst, R.J., 1996b. Deterministic sliding block methods for estimating seismic displacements of earth structures. Soil Dynamics and Earthquake Engineering 15 (4), 255–268.

Cazzuffi, D., Picarelli, L., Ricciuti, A., Rimoldi, P., January 1993. Laboratory investigations on the shear strength of geogrid reinforced soils. In: Cheng, S.C.J. (Ed.), Proceedings of the Geosynthetic Soil Reinforcement Testing Procedures, pp. 119–137. ASTM, STP No. 1190, San Antonio, Texas.

Converse, A.M., Brady, A.G., 1992. BAP: Basic Strong-Motion Accelerogram Processing Software Version 1.0. U.S. Department of the Interior, U.S. Geological Survey, Denver, Colorado, Open-File Report 92-296A, 180 pp.

DiMaggio, F.L., Sandler, I.S., 1971. Material model for granular soils. Journal of the Engineering Mechanics Division, ASCE 97 (EM3), 935–950.

Elias, V., Christopher, B.R., Berg, R.R., 2001. Mechanically Stabilized Earth Walls and Reinforced Soil Slopes Design and Construction Guidelines. FHWA-NHI-00-043. National Highway Institute, Federal Highway Administration, Washington, D.C., 394 pp.

Hallquist, J.O., 1998. LS-DYNA Theoretical Manual. Livermore Software Technology Corporation, Livermore, California, 498 pp.

Hatami, K., Bathurst, R.J., 2000. Effect of structural design on fundamental frequency of reinforced-soil retaining walls. Soil Dynamics and Earthquake Engineering 19 (3), 137–157.

Hirakawa, D., Kongkitkul, W., Tatsuoka, F., Uchimura, T., 2003. Time-dependent stress–strain behaviour due to viscous properties of geogrid reinforcement. Geosynthetics International 10 (6), 176–199.

Huang, C.C., Chou, L.H., Tatsuoka, F., 2003. Seismic displacements of geosynthetic-reinforced soil modular block walls. Geosynthetics International 10 (1), 2–23.

Huang, C.C., Wu, S.H., 2006. Simplified approach for assessing seismic displacements of soil-retaining walls. Part I: Geosynthetic-reinforced modular block walls. Geosynthetics International 13 (6), 219–233.

Huang, C.C., Wu, S.H., Wu, S.H., 2009. Seismic displacement criterion for soil retaining walls based on soil strength mobilization. Journal of Geotechnical and Geoenvironmental Engineering, ASCE 135 (1), 74–83.

IFAI, 2011. Geosynthetics, Specifier's Guide, vol. 28. Industrial Fabric Association International, Roseville, Minnesota, No. 6, 127 pp.

Ko, H.Y., Sture, S., 1981. State of the art: data reduction and application for analytical modeling. In: Yong, R.N., Townsend, F.C. (Eds.), Laboratory Shear Strength Soil. American Society of Testing and Materials, pp. 329–386. ASTM STP 740.

Koseki, J., Munaf, Y., Tatsuoka, F., Tateyama, M., Kojima, K., Sato, T., 1998. Shaking and tilt table tests of geosynthetic-reinforced soil and conventional-type retaining walls. Geosynthetics International 5 (1–2), 73–96.

Koseki, J., Bathurst, R.J., Guller, E., Kuwano, J., Maugeri, M., September 2006. Seismic stability of reinforced soil walls. In: Kuwano, J., Koseki, J. (Eds.), Geosynthetics. Proceedings of the 8th International Conference on Geosynthetics, vol. 1, pp. 51–77. Yokohama, Japan.

Kulhawy, F.H., Mayne, P.W., 1990. Manual on Estimating Soil Properties for Foundation Design. Electric Power Research Institute, Palo Alto, California, EPRI EL-6800, Project 1493-6, 308 pp.

Lee, H.H., Hsieh, C.J., Huang, C.C., Hsu, H.C., September 2002. Dynamic parameters used fro seismic behaviors of MSE-wall. In: Delmas, Ph., Gourc, J.P., Girard, H. (Eds.), Geosynthetics. Proceedings of the 7th International Conference on Geosynthetics, vol. 1, pp. 291–294. Nice, France.

Lee, K.L., Singh, A., 1971. Compaction of granular soils. In: Ninth Annual Symposium on Engineering Geology and Soils Engineering, Proceedings of the 9th Annual Engineering Geology and Soils Engineering Symposium, Boise, Idaho, April 1971, pp. 161–174.

Lee, K.Z.Z., Chang, N.Y., Ko, H.Y., 2010. Numerical simulation of geosynthetic-reinforced soil walls under seismic shaking. Geotextiles and Geomembranes 28 (4), 317–334.

Lee, K.Z.Z., Chang, N.Y., Ko, H.Y., 2011. Reply to the discussion by Ling, H.I. on 'Numerical simulation of gosynthetic-reinforced soil walls under seismic shaking'. Geotextiles and Geomembranes 29 (2), 170–171.

Leshchinsky, D., 1997. Design Procedure for Geosynthetic Reinforced Steep Slopes. US Army Corps of Engineers Waterways Experiment Station, Washington, DC, USACE-WES, Technical Report REMR-GT-23, 35 pp.

Ling, H.I., Leshchinsky, D., Perry, E.B., November 1996. A new concept of seismic design of geosynthetic-reinforced structures: permanent-displacement limit. In: Ochiai, H., Yasufuku, N., Omine, K. (Eds.), Earth Reinforcement. Proceedings of the International Symposium on Earth Reinforcement, vol. 1, pp. 797–802. Fukuoka, Kyushu, Japan.

Ling, H.I., Leshchinsky, D., Perry, E.B., 1997. Seismic design and performance of geosynthetic-reinforced soil structures. Geotechnique 47 (5), 933–952.

Ling, H.I., Mohri, Y., Leshchinsky, D., Burke, C., Matsushima, K., Liu, H., 2005a. Large-scale shaking table tests on modular-block reinforced soil retaining walls. Journal of Geotechnical and Geoenvironmental Engineering, ASCE 131 (4), 465–476.

Ling, H.I., Liu, H., Yoshiyuki, M., 2005b. Parametric studies on the behavior of reinforced soil retaining walls under earthquake loading. Journal of Engineering Mechanics, ASCE 131 (10), 1056–1065.

Liu, H., Wang, X., Song, E., 2011. Reinforcement load and deformation mode of geosynthetic-reinforced soil walls subject to seismic loading during service life. Geotextiles and Geomembranes 29 (1), 1–16.

Matsuo, O., Tsutsumi, T., Yokoyama, K., Saito, Y., 1998. Shaking table tests and analyses of geosynthetic-reinforced soil retaining wall. Geosynthetic International 5 (1–2), 97–126.

Newmark, N.M., 1965. Effects of earthquakes on dams and embankments. Geotechnique 15 (2), 139–160.

NAVFAC, 1986a. Soil Mechanics, Naval Facilities Engineering Command, Design Manual 7.01, Alexandria, Virginia, 388 pp.

NAVFAC, 1986b. Foundations and Earth Structures, Naval Facilities Engineering Command, Design Manual 7.02, Alexandria, Virginia, 279 pp.

Peck, R.B., Hanson, W.E., Thornburn, T.H., 1974. Foundation Engineering, second ed. John Wiley & Sons, Inc., New York, 514 pp.

Rowe, R.K., Ho, S.K., 1998. Horizontal deformation in reinforced soil walls. Canadian Geotechnical Journal 35 (2), 312–327.

Rowe, R.K., Skinner, G.D., 2001. Numerical analysis of geosynthetic reinforced retaining wall constructed on a layered soil foundation. Geotextiles and Geomembranes 19 (7), 387–412.

Siddharthan, R.V., Ganeshwara, V., Kutter, B.L., El-Desouky, M., Whitman, R.V., 2004. Seismic deformation of bar mat mechanically stabilized earth walls. II: Multiblock model. Journal of Geotechnical and Geoenvironmental Engineering, ASCE 130 (1), 26–35.

Sture, S., Desai, C.S., Janardhanam, R., April 1979. Development of a constitutive law for an artificial soil. In: Wittke, W. (Ed.), Numerical Methods in Geomechanics Aachen 1979. Proceedings of the Third International Conference on Numerical Methods in Geomechanics, vol. 1, pp. 309–317. Aachen, W. Germany.

Whitman, R.V., Liao, S., July 1984. Seismic design of gravity retaining walls. In: Eighth World Conference on Earthquake Engineering, vol. 3. Earthquake Engineering Research Institute, San Francisco, California, pp. 533–540.

Zaman, M.M., Desai, C.S., Faruque, M.O., May–June 1982. An algorithm for determining parameters for cap model from raw laboratory test data. In: Eisenstein, Z. (Ed.), Numerical Methods in Geomechanics Edmonton 1982. Proceedings of the Fourth International Conference on Numerical Methods in Geomechanics, vol. 1, pp. 275–285. Edmonton, Canada.